ACS APPLIED MATERIALS & INTERFACES

Forum Article

www.acsami.org

Thermal Control of Nanostructure and Molecular Network Development in Epoxy-Amine Thermosets

Christopher M. Sahagun and Sarah E. Morgan*

School of Polymers and High Performance Materials, The University of Southern Mississippi, Hattiesburg, Mississippi 39401, United States

ABSTRACT: Epoxy-amine resins find wide application as the matrix material of high performance polymer composites because of their favorable mechanical properties, thermal properties and solvent stability. These properties result from the complicated, highly cross-linked molecular network that is characteristic of epoxy-amine thermoset polymers. The connectivity of the molecular network has a strong influence on the physical performance of the finished part. Nonhomogeneity in the network structure can degrade these favorable properties through the introduction of low-energy pathways for solvent penetration or fracture propagation. This work examines the influence of cure temperature on the network-building cross-linking reaction and the subsequent effect on the homogeneity of the cross-linked molecular network. Specific attention is paid to nanoscale variation in the distribution of cross-link density. Thermal, rheological, and spectroscopic techniques are used to monitor key chemical and structural changes during network growth. Atomic force microscopy is used to understand nanoscale fracture behavior in terms of the low energy pathways that result from a nonhomogeneous distribution of cross-link density. The influence of processing-induced changes in molecular connectivity is discussed in terms of observed nanoscale morphology and fracture properties of the cured material.

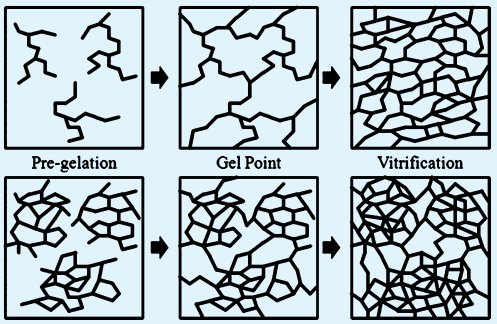

KEYWORDS: *epoxy-amine, thermoset polymer, time−temperature transformation, nanoscale morphology, polymer fracture*

INTRODUCTION

Epoxy-amine systems find wide application as the polymeric matrix of high-performance aerospace composite materials. These systems are characterized by a highly cross-linked molecular network that develops through a step-growth polymerization reaction. The molecular architecture of the resulting network drives important physical performance characteristics such as modulus, thermal response, solvent/water ingress, and fracture behavior.[1−7] Polymerization is usually thermally induced. Modification of the thermal cycle during processing, therefore, provides an opportunity to control molecular network growth and, consequently, the resulting molecular architecture of the fully cured system. Improving the ability to control network architecture provides an attractive opportunity to tune the physical properties of composite matrices from the molecular scale. This has clear benefits for optimizing performance as well as the potential to enable the composite matrix to perform multiple functions. For example, controlling the distribution of free volume within the cross-linked molecular network can provide improved solvent or water resistance.[8] Reducing permeability will then allow the finished part to perform dual roles as a structural member and a moisture barrier, reducing both weight and fabrication complexity. For these advances to be made, however, the influence of processing parameters on the molecular connectivity of the final network must be determined. This work examines the nonhomogeneous molecular network architecture of thermosetting epoxy-amine systems by identifying domains with differing levels of cross-link density, characterizing the influence of processing temperature on the resulting molecular connectivity and relating differences in molecular architecture to bulk fracture properties.

The structure of epoxy-amine thermoset molecular networks strongly influence the physical properties of composite materials. The observation of a distinct, submicrometer nodular morphology in scanning electron micrographs of cured epoxy-amine systems has been reported for years.[9−13] These early reports were corroborated by nonmicroscopic techniques as well.[14−16] These observations sparked an active debate regarding the inherent heterogeneity of the cross-linked molecular network.[17,18] However, it is now accepted by the majority of researchers that epoxy systems do indeed possess a nonhomogeneous molecular network structure. This opinion has been supported by more recent studies making use of small angle neutron scattering and atomic force microscopy to interrogate epoxy systems.[19−22] These studies show nonhomogeneous domains similar in size and shape to the heterogeneities observed in this work. Multiple researchers have proposed that these nodular structures are composed of regions of relatively higher cross-linking surrounded by an interstitial phase of relatively lower cross-link density and that opinion is shared by this work.[1,15,21,23−25]

Received: October 31, 2011
Accepted: January 18, 2012
Published: January 25, 2012

 © 2012 American Chemical Society dx.doi.org/10.1021/am201515y | *ACS Appl. Mater. Interfaces* 2012, 4, 564−572

Recent work in our laboratory has tracked the growth of individual nodular structures with respect to network development in isothermally cured samples by monitoring cure-induced changes in the nanoscale morphology of the fracture surface via nanoindentation and atomic force microscopy.[26,27] This work has demonstrated that the morphology of the fracture surface is directly related to the structure of the underlying molecular network, specifically with relation to the distribution of cross-link density within the molecular network. The commonly observed nodular morphology was found to appear only in samples that had been cured beyond the gel point and development of the nanostructures was monitored between gelation and the onset of vitrification. Fracture surface morphology was correlated to molecular network development by interpreting the fracture surface as the "critical fracture manifold".[28−30] The critical fracture manifold is the virtual surface within a sample that traces the lowest energy pathway for separating the molecular network into two independent subnetworks. For the case of a highly cross-linked glassy elastic material, such as a cured epoxy, the propagating fracture surface follows a pathway that involves breaking the minimum number of strong covalent bonds. Therefore, the propagating crack tip will preferentially travel through regions with relatively lower levels of covalent bonding (that is, with lower cross-link density) while preserving regions with higher a concentration of covalent bonds at the fracture surface. A similar analysis has been used to explain why propagating crack tips preferentially propagate around spherulites in polypropylene and tend to propagate along interlaminar boundaries in nylon-6.[31,32] In this way, the propagating crack tip functions as a nanoscale "probe" for variation in cross-link density and these variations are visible in the topography of the fracture surface with regions of higher cross-link density appearing as nodular structures.

The present work investigates the influence of processing temperature on the development of the nanoscale morphology during the cure process. These molecular-scale factors are then used to explain measured differences in bulk fracture behavior of the cured epoxy-amine system. In this way, bulk physical properties can be related to molecular structure and the influence of cure temperature on both molecular-scale and bulk-scale parameters can be understood. To the best of our knowledge, a systematic study of the relationship of processing conditions with nanoscale morphology development and its correlation with mechanical properties has not been reported. Providing increased understanding of the factors that control the development of the network, as well as its final nanoscale morphology, will help to improve capabilities to predict and control composite properties for aerospace applications.

EXPERIMENTAL METHODS

Materials. Diglycidyl ether of bisphenol A (Epon 828) was purchased from E.V. Roberts Co. (Carson, CA). Epon 828 is a low-molecular-weight difunctional epoxy oligomer that was received as a clear viscous liquid. 3,3′-diaminodiphenyl sulfone (DDS) was purchased from Tokyo Chemical Industry Company. DDS is a tetrafunctional aromatic amine that was received as a fine white powder. The chemical structures of the epoxy component and the amine curing agent are shown in Figure 1. All materials were used as received.

Sample Preparation. *Resin Mixing.* One hundred grams of Epon 828 were placed in a standard lab beaker that was immersed in an oil bath heated to 130 °C. The Epon 828 was allowed to warm for 2 min and then 32.6 g of DDS were added. These amounts were chosen based on the difunctionality of the Epon 828 and the tetrafunctionality

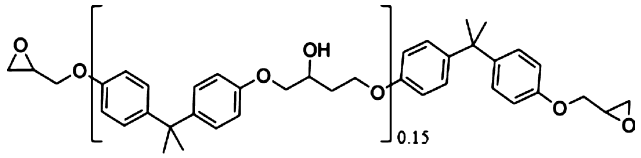

diglycidyl ether of bisphenol A

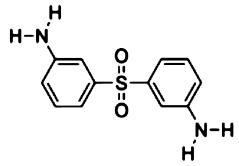

3,3'-diaminodiphenyl sulfone

Figure 1. Molecular structure of diglycidyl ether of bisphenol A and 3,3′-diamino diphenyl sulfone.

of the DDS in order to yield a 1:1 ratio of the reactive groups. This ensured that, theoretically, 100% of each reactive species would be consumed. The mixture was stirred mechanically at 130 °C under normal atmospheric conditions. Each batch was allowed to stir for 20 min at which point the mixture was observed to be a clear, low viscosity liquid. The mixed resin was then immediately prepared for specific tests. To accurately compare network development at different curing temperatures, new batches of resin were mixed for each test to ensure that all experimentation was conducted on material that had been heated at 130 °C for 20 min.

Determination of Time to Gelation. The time to gelation for each reaction temperature was determined by monitoring the evolution of the dynamic shear moduli during the curing reaction using an ARES Rheometer from TA Instruments (New Castle, DE) equipped with a heating oven that held the sample isothermally at the desired cure temperature for the duration of the test. After mixing, the liquid Epon 828/DDS mixture was poured directly onto 25 mm aluminum parallel plates that had been preheated to the desired cure temperature. Care was taken to avoid the introduction of air bubbles. Testing was conducted with a gap of 1 mm. The ARES rheometer is capable of MultiWave testing which allows multiple frequencies to be tested simultaneously over 2 orders of magnitude.[33] This is advantageous as it reduces the amount of time required for measurement. Each test took around 25 s, meaning that cure progressed to some degree during the time required to complete the measurement, however this time is small compared to the overall time the sample was monitored, thus any change in the network from the beginning to the end of each individual test is small enough not to affect the measurement to a large degree. Measurements were made at 0.1% strain as this was sufficiently low to avoid non-Newtonian effects and network breakdown. Initial tests were conducted to ensure all measurements were made in the linear viscoelastic region. The storage (G') and loss (G'') moduli were measured every 2 min at frequencies of 0.5, 1, and 50 rad/s simultaneously. These values were used to calculate the loss tangent ($\tan \delta$)

$$\tan \delta = \frac{G''}{G'}$$

The measured values of the tan δ were plotted as a function of time and the time to gelation was determined by noting the point at which the measured value of tan δ was independent of the measurement frequency.[34,35] This process was repeated for each reaction temperature to determine the time to gelation at a variety of cure temperatures.

Determination of Time to Onset of Vitrification. A Q100 differential scanning calorimeter (DSC) from TA Instruments (New Castle, DE) was used to monitor the evolution of the glass transition temperature with cure time. Approximately 12 mg of the mixed resin was placed into hermetically sealed aluminum DSC pans. Samples were held at the desired cure temperature in the DSC for

dx.doi.org/10.1021/am201515y | ACS Appl. Mater. Interfaces 2012, 4, 564−572

predetermined lengths of time and then thermally scanned from −10 to 200 °C at 20 °C per minute. Data was analyzed with TA Universal Analysis v.4.5A. The T_g was taken as the inflection point of the exotherm. The onset of vitrification was accepted as the point where the T_g of the sample no longer increased with additional cure time indicating that the cross-linking reaction had slowed significantly.[36] This point was easily identified by plotting the measured T_g as a function of cure time and noting the time at which the plot showed an obvious change in slope. Because of time constraints, the onset of vitrification was determined rheometrically for samples cured at low temperatures (time to vitrification greater than 500 min). This was done by identifying the time at which the storage modulus reached a plateau value.[37]

Determination of the Onset of Vitrification. A Q500 TGA from TA Instruments (New Castle, DE) was used to identify the onset of degradation. Approximately 25 mg of uncured resin was placed in a platinum TGA pan and held isothermally at a desired temperature while monitoring any reduction in mass. Data was analyzed with TA Universal Analysis v.4.5A. The onset of degradation was taken to be the point where the sample was observed to have lost 15% of the initial mass.

Determination of Monomer Conversion. Monomer conversion was monitored by real-time transmission near-infrared spectroscopy (NIR). After mixing according to the procedure described above, a small amount of resin was sandwiched between two borosilicate glass microscope slides using a PTFE spacer around 3 mm thick to ensure a reasonably consistent path length. A Nicolet 6700 spectrometer from Thermo Scientific (Waltham, MA) equipped with a heating cell was used to monitor changes in absorption in the region 10 000−4 000 cm^{-1} during isothermal cure at each experimental temperature. 32 scans were made during each sampling interval with a resolution of 4 cm^{-1}. Spectral analysis was performed with OMNIC v.7.3 software from Thermo Electron Corporation. The concentration of primary, secondary, and tertiary amine was determined as a function of cure time from the area of the absorption bands listed in Table 1.

Table 1. Initial Molar Concentrations, Molar Absorptivities, and Wavenumbers of the Absorption Bands Used to Quantify NIR Spectra for the Sample Cured at 150°C[a]

chemical group	molar absorptivity (kg mol^{-1})	initial molar concentration (mol kg^{-1})	wavenumbers (cm^{-1})
phenyl	7.0	6.41	4605−4630
epoxy		3.92	4510−4550
1° amine		1.98	4510−4550
1° amine	0.5	1.98	5100−5040
1° amine	2.4	1.98	6720−6520
2° amine	1.1		6720−6520

[a]The initial molar concentration and wavenumbers of the absorption bands used to calculate concentration were identical for all cure temperatures; however, the calculated molar absorptivity varied slightly with temperature.

Changes in concentration of each amine species were calculated according to Beer's law following methods capable of discriminating between the concentration of primary, secondary and tertiary amine that are described elsewhere.[38,39] The difficulty of preparing samples with identical path lengths was overcome by using the phenyl group band at 4605−4630 cm^{-1} as an internal standard to normalize the integrated peak areas. The absorption coefficients required to calculate concentration according to Beer's law are both frequency-specific and temperature dependent and therefore were calculated for each chemical species of interest at the frequency ranges listed in Table 1 for each cure temperature. Table 1, as an example, shows the calculated values for the sample isothermally cured at 150 °C (values calculated for other cure temperatures were similar and are not shown).

Epoxy concentration at time = t was calculated according to the following relationship:

$$[EP]_t = [EP]_0 - [1°amine]_t - 2[2°amine]_t$$

where $[EP]_t$ is the concentration of epoxy groups at the measurement time, $[EP]_0$ is the initial concentration of epoxy groups $[1°amine]_t$ and $[2°amine]_t$ are the concentration of primary and secondary amine at the measurement time, respectively.

This relationship is based upon the assumption that the etherification reaction of the epoxy groups by hydroxyl groups produced during the reaction makes only a minor contribution to the total epoxy conversion. The reaction of an epoxide with a hydroxyl group has a higher activation energy than the reaction of an epoxide with an aromatic amine and therefore is less favored thermodynamically.[40] Studies of a model system consisting of monofunctional 1,2-epoxy-3-phenyoxypropane cured with 4,4,′-diamino diphenyl sulfone showed that the etherification reaction generally occurs after extended cure times at elevated temperatures and during the late stages of reaction in systems with excess epoxy.[41,42] A study of the reaction of a model phenylglycidyl ether molecule with various amine species found a negligible reaction between the epoxy and hydroxyl groups produced during the reaction.[43] Nevertheless, the possibility of the etherification reaction contributing to the cross-linking reaction to some degree should not be discounted, especially in samples cured at the highest reaction temperatures.

Concentration of secondary amine was determined by deconvolution of the absorbance at 6520−6720 cm^{-1} according to the following relationship:

$$A_t = \varepsilon_{1°}[1°amine]_t + \varepsilon_{2°}[2°amine]_t$$

where A_t is the total band area at time t, $\varepsilon_{1°}$, and $\varepsilon_{2°}$ are the molar absorptivities of the primary and secondary amines at 6520−6720 cm^{-1}, respectively, and $[1°amine]_t$ is the concentration of primary amine at time t calculated from its nonconvoluted absorption band at 5040−5100 cm^{-1}. The tertiary amine concentration was calculated from the balance of primary and secondary amine consumed and produced

$$[TA]_t = [PA]_0 - [PA]_t - [SA]_t$$

Where $[TA]_t$ is the concentration of tertiary amine at time t, $[PA]_0$ is the initial concentration of primary amine and $[PA]_t$ and $[SA]_t$ are the concentrations of the primary and secondary amine at time t, respectively.

Fracture Testing. Fracture test specimens were produced by pouring the mixed Epon 828/DDS resin into 75 mm × 15 mm × 7 mm silicone molds. The molds were preheated to the desired temperature and the samples were then isothermally cured up to the onset of vitrification (as determined by prior DSC or rheometric analysis). Some samples were postcured by holding them at 200 °C for an additional 120 min.

Fracture testing was conducted according to ASTM D-5045.[44] Low cure temperature samples were extremely brittle and therefore it was not possible to reliably induce a precrack. Therefore, it was decided to not precrack any of the specimens, despite the protocol called for in ASTM D-5045. For this reason, the fracture test results reported here are best viewed as a means to compare the fracture toughness of samples within the experimental set fabricated for this work.

The resulting fracture surfaces were saved for imaging via atomic force microscopy.

Atomic Force Microscopy. The fracture surface morphology of the fracture specimens was characterized with a Dimension 3000 atomic force microscope (AFM) from Veeco Instruments (Santa Barbara, CA) equipped with an optical positioning system. Surface topography images were made with a silicon probe with a 125 μm long cantilever and a nominal spring constant of 40 N/m operated in tapping mode at its resonance frequency of around 370 kHz. The tip had a nominal radius of curvature of 8 nm. The cantilever's tapping amplitude during imaging was maintained at around 85−90% of the free amplitude to minimize cantilever-induced surface deformation while also allowing

adequate tracking of the sample surface. AFM imaging was conducted under ambient conditions in a temperature (20 °C) and humidity (40–45%) controlled room.

The fracture surfaces that were created during the fracture toughness experiments were cut to size using a high speed diamond saw. The cutting process was not found to noticeably contaminate the imaging surface. The samples were then affixed to an AFM stage puck with putty. The fracture surface samples obtained from the fracture testing described above were not macroscopically smooth, as is generally the case for samples interrogated via AFM. The optical positioning system of the AFM provides a magnified image of the sample surface and this magnified image was used to find a suitably flat imaging region. Images were preferentially taken at the "mirror" region of the fracture surface. However, the mirror region was inaccessible for some samples so images were instead made on the "mist" region of fracture. Initial studies showed that identical nanoscale morphologies are seen on the mirror, mist, and hackle regions of the fracture surface, despite the differences in macroscopic morphology. This indicates that these structures result from the network architecture, not the fracture process.

750 nm x 750 nm areas were scanned at a rate of 0.75 Hz with a resolution of 512 × 512 pixels. Multiple areas were scanned for each sample and figures presented here show representative morphology. Images and statistical quantities were processed with Gwyddion v.2.24 SPM analysis software. Image processing was limited to data leveling by plane subtraction and the correction of scan line artifacts. Root mean square (RMS) roughness for each sample was calculated according to ASME B46.1–1995.[45] RMS roughness describes the height deviation of individual data points (pixels) measured from the mean surface-height plane and is given by the following equation

$$R_{\mathrm{RMS}} = \sqrt{\frac{1}{N}\sum_{j=1}^{N} r_j^{\,2}}$$

where N is the total number of pixels and r_j is the vertical distance of pixel j from the mean surface-height plane.

RESULTS AND DISCUSSION

Time–Temperature Transformation Behavior of the Epoxy-Amine System. The isothermal transformation behavior of the epoxy-amine system is illustrated in Figures 2 and 3. Figure 2 shows the time required to reach the gel point for a series of samples cured at different temperatures. Figure three shows the time required to reach the onset of degradation and vitrification. Degradation was not observed within the measurement time at temperatures below 260 °C. Note that samples cured at 50 °C vitrified prior to reaching their gel point. This cure temperature produced a brittle, glassy solid that was entirely soluble in acetone and was found to melt at elevated temperatures in much the same way as a thermoplastic material.

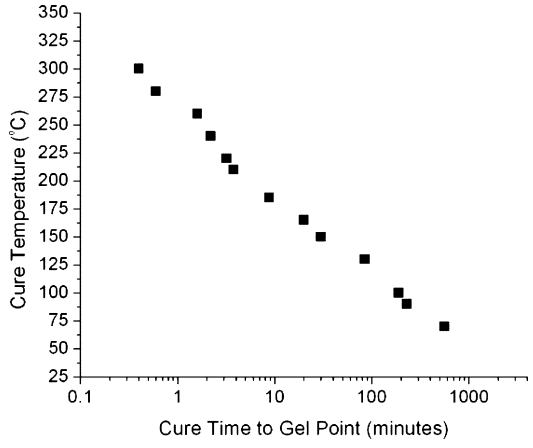

Figure 2. Cure time required to reach the gel point for a series of cure temperatures.

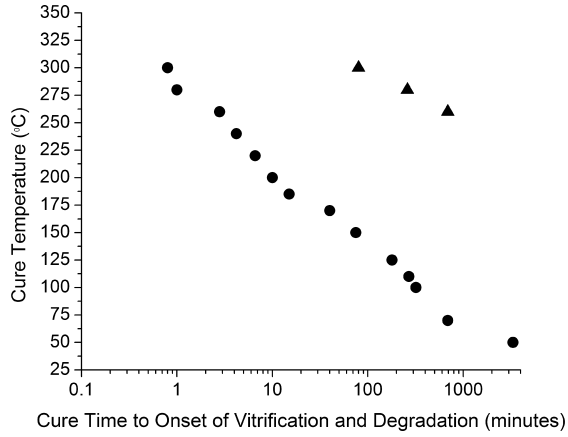

Figure 3. Cure time required to reach the onset of vitrification (●) and degradation (▲) for a series of cure temperatures.

Network growth can be divided into three different stages, each with different modes of network growth. Prior to the gel point, the system consists of unreacted monomer and low molecular weight oligomeric species. During this pregelation stage the network-building reaction is largely under chemical control as unreacted species are able to freely diffuse to active reaction sites. The gel point marks the initial appearance of an infinite molecular weight network and the beginning of the main stage of network growth. The growing network begins to restrict diffusion of unreacted species and this diffusion control becomes more pronounced as the sample approaches vitrification. The onset of vitrification marks the effective end of network growth as the cross-linked network prevents diffusion of unreacted species to active reaction sites. Elevated temperature is required to drive further monomer conversion.

The pregelation, main stage and postvitrification phases of network development each present different physical and chemical reaction environments for the network building reaction. The growing network begins to restrict the transport of mass at the gel point. Large fragments are the first to be diffusion restricted with smaller and smaller fragments becoming diffusion restricted as the network develops. The epoxy-amine reaction mechanism can be complicated, with the potential to form cross-links not only by reaction of the epoxy with the amine, but also through etherification and, at elevated temperatures, epoxy–epoxy reactions.[46] Increasing concentration of hydroxyl groups resulting from ring-opening of the oxirane induces a degree of autocatalytic behavior.[47] Additionally, primary and secondary aromatic amines show different reactivities, and thus their relative concentration changes throughout the course of the reaction.[47,48] This evolution of the reaction environment alters the way mass is added to the growing network. It is reasonable to anticipate that these changes may be a driving force for the formation of a nonhomogeneous final network architecture.

Influence of Cure Temperature on Molecular Structure. Evolution of the molecular structure during cure was monitored by real-time NIR. Figure 4, from a sample cured at 150 °C, is typical of the spectra collected. Figure 5 shows concentration curves of primary, secondary and tertiary amine

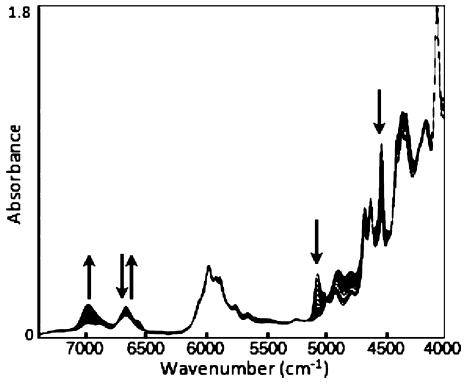

Figure 4. Real-time NIR spectra for a sample cured at 150 °C. Arrows indicate change in peak height during cure. Steady concentration associated with the phenyl ring is seen at 4630−4605 cm^{-1}, decrease in epoxide concentration is seen at 4550−4510 cm^{-1}, decrease in 1° amine concentration is seen at 5100−5040 cm^{-1}, increase and then decrease in 2° amine concentration is seen at 6720−6520 cm^{-1}, increase in hydroxyl concentration is seen at 6900−7075 cm^{-1}.

species as a function of cure time for samples cured at 90, 150, and 185 °C up to the onset vitrification. The effect of cure temperature on the conversion of monomer can be clearly seen in these figures. At 90 °C (Figure 5a), concentration changes linearly for all amine species. The concentration of tertiary amine increases nearly concurrently with the concentration of secondary amine. At 150 °C (Figure 5b), the concentration of secondary amine increases quickly to reach a maximum concentration after around 50 min of cure. Tertiary amine conversion shows an apparent induction period with little tertiary amine produced until approximately 75% of the primary amine has been converted to secondary amine. At 185 °C, primary amine shows nearly complete conversion within 20 min. The secondary amine again shows a maximum concentration, although only about one-third of the maximum concentration achieved at 150 °C. Interestingly, the concentration of tertiary amine increases nearly concurrently with secondary amine concentration during the first 5 minute of cure, similar to the conversion behavior observed for the sample cured at 90 °C.

The amine conversion data provides valuable information about the molecular structure of the network at different stages of network development. A primary amine reacts with an epoxy unit to produce a secondary amine, which yields a linear segment. The resulting secondary amine will subsequently react with a different epoxy unit to produce a tertiary amine which yields either a branch or a cross-link, depending on the prior connectivity of the epoxy unit. A high concentration of secondary amine, therefore, corresponds to a mostly linear molecular architecture while a high concentration of tertiary amine indicates a branched or cross-linked structure. In this way, NIR spectroscopy can be used to discern the molecular architecture of the developing network at different stages of development.

Determining the ratio of linear segments compared to the number of branched segments (that is, the ratio of secondary amine to tertiary amine) is particularly helpful for understanding how the network grows during the initial pregelation stage of network development. This method is advantageous as the rates of linear and branched segment production can be measured directly from the plots in Figure 5. This rate is distinct from the chemical conversion rate of the amine species,

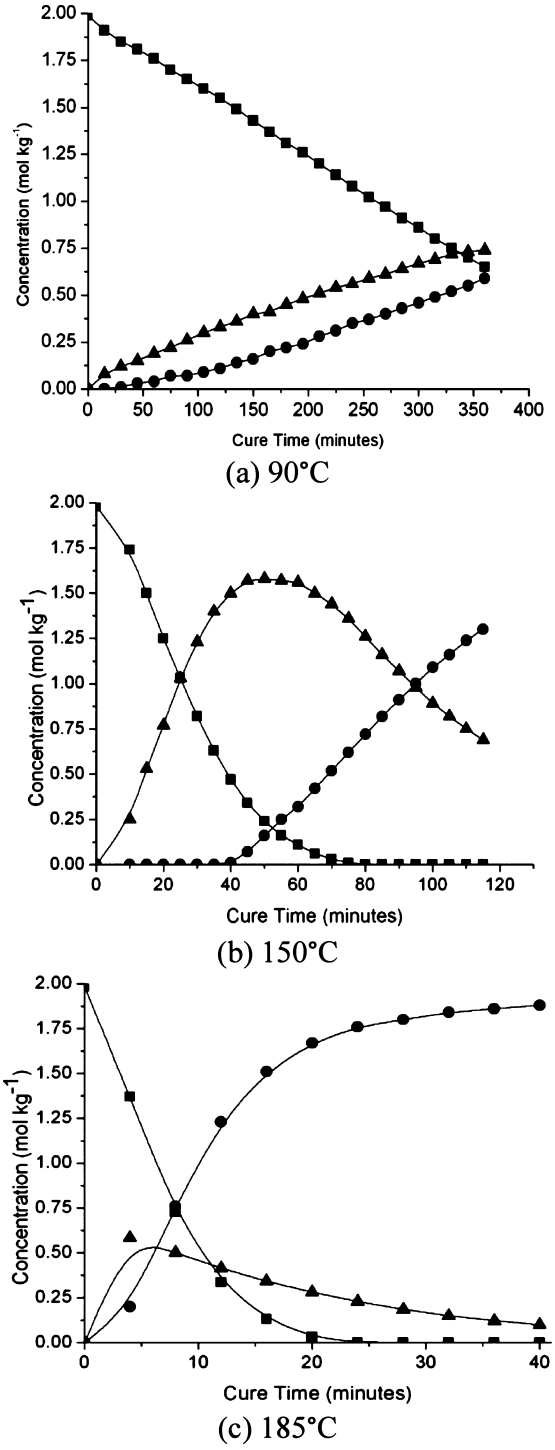

Figure 5. Concentration of primary amine (■), secondary amine (▲), and tertiary amine (●) as a function of cure time. (a) 90 °C, gel point at 231 min, vitrification at 316 min, final epoxy conversion was 49%. (b) 150 °C, gel point at 30 min, vitrification at 75 min, final epoxy conversion was 84%. (c) 185 °C, gel point at 9 min, vitrification at 15 min, final epoxy conversion was 94%.

which can be quite complicated to determine.[46] The rate of production of each type of connection point is a direct measurement from the conversion curves shown in Figure 5 and is not complicated from the action of autocatalytic behavior, differences in primary and secondary amine reactivities, and the noninstantaneous shift from chemical to

dx.doi.org/10.1021/am201515y | ACS Appl. Mater. Interfaces 2012, 4, 564−572

diffusion control. The production rate of linear and branched/cross-linked segments depends only on measured concentration and no rate equation is necessary for its determination.

Table 2 shows the production rate of linear segments and branched/cross-linked segments during the pregelation stage of network development. These values were calculated from the initial slope of the concentration of secondary and tertiary amine plotted in Figure 5. Comparison of the rates of production of secondary and tertiary amine reveals differences in the molecular architecture of the nanogels formed during the initial stages of the cure reaction. As expected, overall segment production rates are found to increase with increasing temperature. However, the relative rate of production of linear segments and branched/cross-linked segments within a sample is seen to vary with temperature. Samples cured at 185 and 90 °C produce linear and branched/cross-linked segments at, to a first approximation, similar rates, while samples cured at 150 °C produce linear segments more than ten times faster than branched/cross-linked segments. Autocatalysis of the secondary amine by hydroxyl groups reaction at low reaction temperatures (below 100°) has been reported, which may be responsible for the seemingly contradictory behavior of a faster secondary amine conversion rate at both lower and higher temperatures.[48] Comparing segment production rates shows that samples cured at 150 °C produce initial nanogels with a mostly linear molecular structure, whereas the nanogels produced in samples cured at 90 and 185 °C take on a more cross-linked or branched molecular architecture.

Table 2. Rate of Development of Linear and Branch/Crosslink Segments during the Pre-Gelation Stage of Cure As Determined by Rate of Production of Secondary Amine (Linear Segment) and Rate of Production of Tertiary Amine (Branch/Cross-Link)

	rate (mol kg^{-1} min^{-1})		
segment	90 °C	150 °C	185 °C
linear	0.0037	0.0403	0.1398
branch/cross-link	0.0014	0.0031	0.1115

Influence of Cure Temperature on Fracture Surface Morphology. Topographic AFM images of fracture surfaces of the epoxy-amine system are shown in Figure 6. Each sample was cured slightly beyond the onset of vitrification and fractured with a universal test frame. Previously, we conducted nanoindentation studies in order to understand the influence of the viscoelastic nature of the polymer on the resulting fracture surface.[27] These studies demonstrated that the observed nodular morphology is indeed a function of the underlying network structure rather than an artifact of some viscoelastic effect. This prior work indicates that the AFM images shown in Figure 6 highlight regions of relatively higher cross-link density that were left at the fracture surface as the propagating crack tip deviated to follow the lowest energy fracture pathway through regions with relatively lower cross-link density. Rms roughness values for each cure temperature are shown in Figure 7.

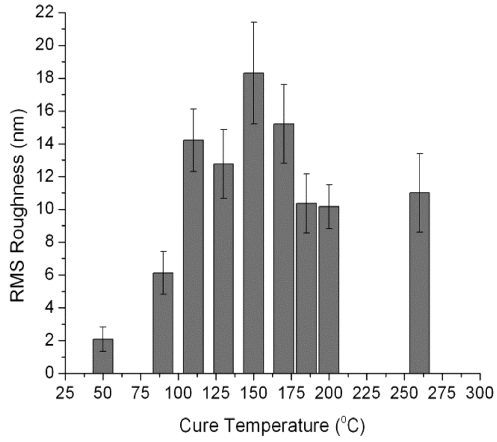

Figure 7. Rms roughness of the fracture surface of samples isothermally cured to the onset of vitrification at various temperatures.

Figure 6a, cured at 50 °C, shows the fracture surface of a sample that vitrified without gelling. This surface appears similar to that observed in AFM images taken of samples where cure has been arrested prior to gelation.[27,49] The RMS roughness is quite low, indicating that the surface is planar. This high planarity is due to the lack of an infinite weight

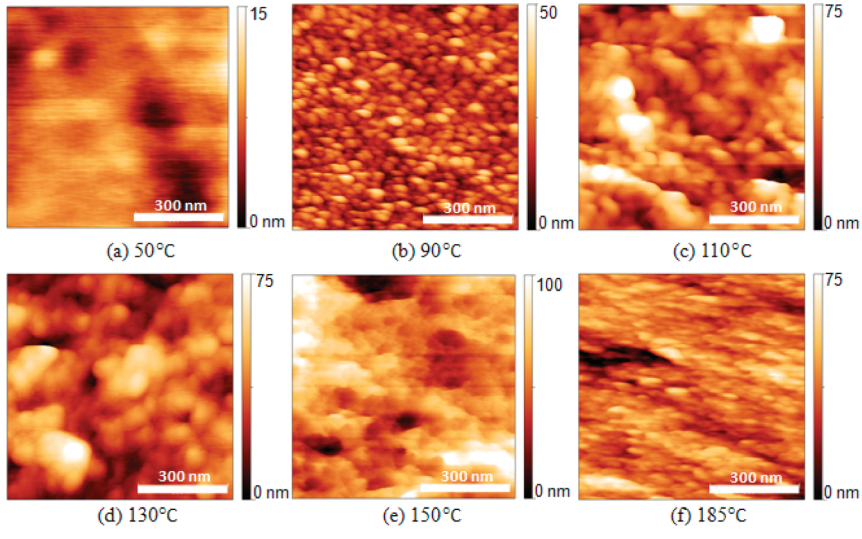

Figure 6. Topographic AFM images of samples isothermally cured to the onset of vitrification at various temperatures.

dx.doi.org/10.1021/am201515y | ACS Appl. Mater. Interfaces 2012, 4, 564–572

molecular network to present a barrier to crack tip propagation. Figure 6b, from a sample cured at 90 °C, distinctly shows the nodular morphology commonly observed in epoxy systems.[19,20] This sample consists of cross-linked nodules around 50 nm in diameter surrounded by an interstitial region that likely contains a high concentration of unreacted material as overall conversion is very low (49% epoxy conversion). Images c and d in Figure 6, cured at 110 and 130 °C, respectively, show similar morphology, and significant increases in surface roughness (Figure 7). These two morphologies illustrate the transition from the distinct, regular nodular structures seen in samples cured at 90 °C to the very rough fracture surface found in samples cured at 150 °C. It is difficult to discern nodular structures in Figure 6e, cured at 150 °C. Rather, a very rough fracture surface is observed. Figure 6f shows the fracture surface morphology of a sample cured at 185 °C. The nodular nanostructures are observed, although they appear less distinct and smaller in diameter (only around 30 nm) in comparison to those observed at lower cure temperatures.

Interpreting the cure temperature-dependent morphology of these fracture surfaces in light of the differences of initial molecular architecture determined by NIR analysis provides insight as to how this nanoscale morphology develops. Both Figure 6b, cured at 90 °C, and Figure 6f, cured at 185 °C show regions of higher cross-link density surrounded by an interstitial region of relatively lower cross-link density. Figure 6c, cured at 150 °C, does not show the well-defined nodular structure. NIR analysis shows that samples cured at 90 and 185 °C develop linear and cross-linked segments nearly simultaneously, while the sample cured at 150 °C develops primarily linear structures initially, with significant cross-linking/branching only at later stages of the reaction. The effect of this type of molecular network growth is shown schematically in Figure 8. The top

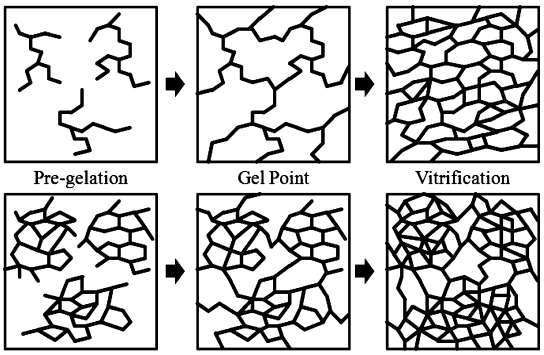

Figure 8. Schematic showing the effect of two different modes of network growth.

scheme shows the type of molecular network expected if the initial microgels develop a linear architecture. These linear segments extend until they eventually connect at the gel point, at which point unreacted species cross-link this "skeleton network" by converting the linear secondary amine to tertiary amine. This behavior is supported by the conversion plot shown in Figure 5b, where the initial high concentration of secondary amine indicates a mostly linear structure during the pregelation stage of cure, whereas the majority of cross-links form during the main stage of network growth. This type of network growth is expected to produce a more homogeneous network structure. The bottom scheme shows the type of molecular network architecture expected if the microgels develop linear segments and cross-links nearly simultaneously. Cross-linked microgels grow in size until they contact at the gel point, at which point chemical bonds are formed at the interface of individual structures. This type of network growth would be likely to produce nonhomogenous network connectivity as individual cross-linked microgels are too massive to diffuse significantly as the system approaches vitrification. This behavior is supported by the conversion plots shown in panels a and c in Figure 5, where branched or cross-linked segments are seen be created at similar rates.

The fracture surfaces shown in Figure 6 reflect the differences in molecular connectivity that will result from the two different modes of molecular network development. The remnants of the initial cross-linked microgels can still be seen as the nodular morphology observed in images b and f in Figure 6. These samples did not form homogeneous networks, as evidenced by the regular, repeating higher cross-linked domains observed at the critical fracture manifold. While both figures show evidence of the nodular morphology, there are clear differences in the regularity and size of the nodular structures. One possible explanation for this is the increased contribution of the etherification reaction to molecular network formation that should be expected at the higher curing temperature of the sample shown in Figure 6f. Figure 6e shows little residual evidence of nodular regions of higher cross-link density in agreement with the structure analysis from NIR data. The increase in roughness indicates that the propagating crack tip now deviates strongly to follow the lowest-energy propagation pathway. The linear molecular growth of the initial microgels enables the formation of larger homogeneous domains in the network structure rather than the smaller, regularly spaced domains of relatively higher and lower cross-link density seen at the fracture surface of samples cured at 90 and 185 °C (Figure 6b, f, respectively). This nanoscale difference in fracture behavior is reflected in bulk measurement of the fracture toughness.

Influence of Molecular Connectivity on Macroscopic Fracture Behavior. Fracture testing provides a way to characterize the interfacial connectivity of individual nanostructures. Figure 9a illustrates the resistance to fracture for a series of samples cured at different temperatures as determined by the fracture toughness. Each sample was cured to the onset of vitrification as measured either rheometrically or by DSC. Samples cured between 150 and 185 °C show the highest resistance to fracture while samples cured at 90 °C show the lowest resistance to fracture. The high fracture toughness values of samples cured at 150 °C are a result of the more homogeneous network structure as observed by AFM interrogation of the critical fracture manifold. The low fracture toughness values of samples cured at 90 °C are a consequence of the high heterogeneity in the network structure observed by AFM interrogation of the critical fracture manifold.

The resistance to fracture is influenced by molecular connectivity which, in turn, is influenced by monomer conversion. Samples cured at 90 °C only underwent 84% epoxy conversion and show the most heterogeneity in the network and also the lowest fracture toughness. The under-cross-linked internodular domain that serves as the low-energy fracture pathway likely consists of high amounts of this unreacted material. Postcuring drives epoxy conversion of this sample to nearly 100% and this increased molecular connectivity is reflected in the large increase in fracture toughness shown in Figure 9b. Figure 10 shows topographic

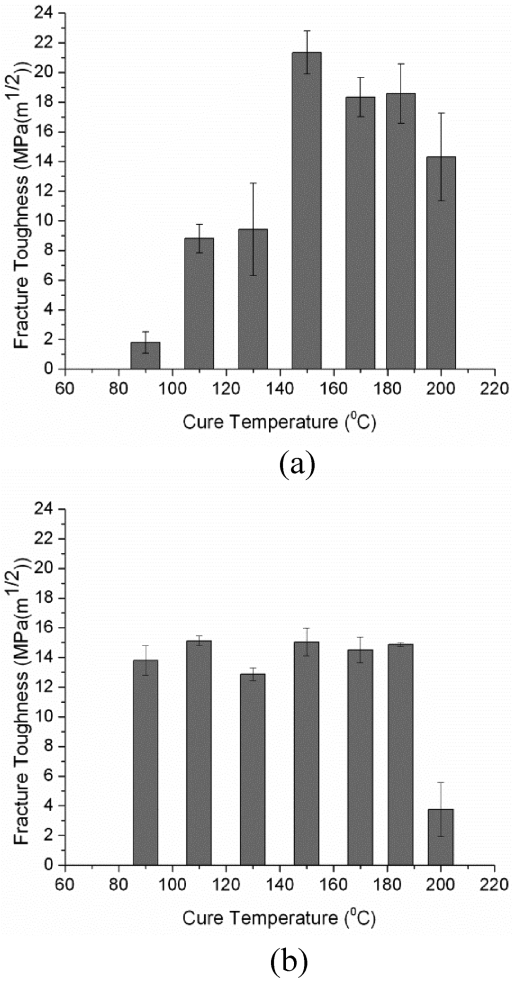

Figure 9. Fracture toughness of samples cured at different temperatures. (a) shows values for isothermally cured samples, (b) shows values for samples postcured at 200 °C for 120 min.

AFM images of a sample cured at 90 °C with and without a postcuring treatment. The clear nodules observed in Figure 10a (no postcuring) are much less distinct after postcuring. Additionally, there is an indication that postcuring causes individual structures begin to coalesce into larger structures, such as the large structure seen at the right side of 10b. This is indicative of increased connectivity which causes the propagating crack tip to deviate around these new regions of relatively higher cross-link density.

Postcuring drove epoxy conversion to nearly 100% in all samples, regardless of initial cure temperature. Figure 9b shows similar fracture toughness values for each sample after postcuring (except for the sample initially cured at 200 °C which visually appeared to have undergone thermal degradation during the postcuring treatment). Prior to postcuring, epoxy conversion was nearly 100% for the sample cured at 200 °C and the fracture toughness was around 14 MPa ($m^{1/2}$). Figure 9b shows that this appears to be a limiting value for the fracture toughness of fully cured systems as all samples (aside from the degraded 200 °C sample) show nearly identical values at near 100% conversion, regardless of initial cure temperature. Samples cured at 150, 170, and 185 °C (with 84, 88, and 94% epoxy conversion, respectively) show lower fracture toughness values after postcuring. This may indicate an increased likelihood for brittle fracture associated with a decrease in free volume as cross-link density increases during postcure. Alternatively, it could be rooted in thermal degradation similar to what was observed for samples initially cured at 200 °C.

CONCLUSIONS

The molecular architecture of epoxy-amine systems is temperature-dependent. Reaction temperature influences the ratio of the production rate of linear molecular segments compared to cross-linked or branched molecular segments in the nanogels that form during the initial, pregelation stage of the network development reaction. The production of significantly more linear segments yields mostly linear nanogels which grow in size until the gel point. After gelation, mass is added to this "skeleton network" up to the onset of vitrification. This type of molecular network development yields a more homogeneous network structure as shown by nanoscale interrogation of the critical fracture manifold and this more homogeneous network yields higher fracture toughness. The production of branched or cross-linked segments at about the same rate as linear segment production yields nanogels with internal cross-links which grow in size until the gel point. The remnants of these structures can be seen at the critical fracture manifold, which indicates a less homogeneous network structure consisting of domains of higher cross-link density surrounded by an interstitial region of relatively lower cross-link density. The apparent homogeneity of the molecular network can be improved by postcuring above the glass transition temperature

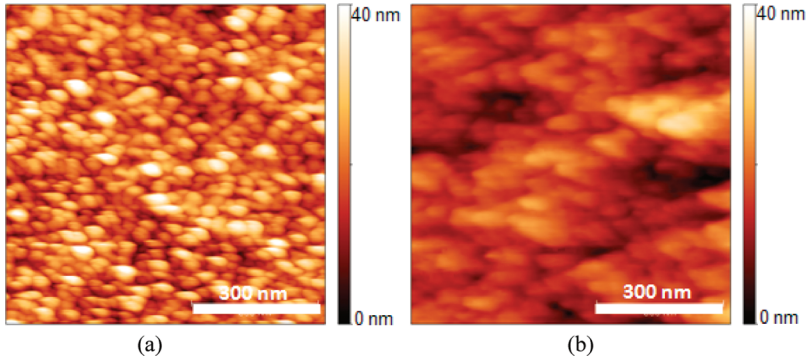

Figure 10. Topographic AFM images of a sample cured at 90 °C to the onset of vitrification (a) prior to postcure and (b) after postcuring at 200 °C for 120 min.

dx.doi.org/10.1021/am201515y | ACS Appl. Mater. Interfaces 2012, 4, 564–572

of the material to allow unreacted species to increase molecular connectivity within this interstitial region.

These results indicate that understanding of both the development of the network and its final nanoscale morphology is important in predicting and controlling composite properties related to nonhomogeneities, such as solvent ingress and fracture toughness. This type of analysis can be expanded to other classes of polymer composite systems. It is our hope that the experiments will help to inform molecular dynamic simulations in our own and other laboratories to accelerate development of improved composite structures.

AUTHOR INFORMATION

Corresponding Author

*E-mail: Sarah.Morgan@usm.edu.

Notes

The authors declare no competing financial interest.

ACKNOWLEDGMENTS

This work was supported by the Office of Naval Research, Award N00014-07-105.

REFERENCES

(1) Feng, J.; Berger, K.; Douglas, E. *J. Mater. Sci.* **2004**, *39*, 3413.
(2) Choi, S; Douglas, E. *ACS Appl. Mater. Interfaces* **2010**, *2*, 934.
(3) Haris, A; Adachi, T; Araki, W. *Mater. Sci. Eng., A* **2008**, *A496*, 337.
(4) Yung, K; Zhu, B; Yue, T; Cie, C. *J. Appl. Polym. Sci.* **2010**, *116*, 518.
(5) Ellis, B; Found, M; Bell, J. *J. Appl. Polym. Sci.* **2001**, *82*, 1265.
(6) Lesser, A; Crawford, E. *J. Appl. Polym. Sci.* **1997**, *66*, 387.
(7) Ochi, M; Tsuyuno, N; Sakaga, K; Nakanishi, Y; Murata, Y. *J. Appl. Polym. Sci.* **1995**, *56*, 1161.
(8) Jackson, M; Kaushik, M; Nazarenko, S; Ward, S; Maskell, R; Wiggins, J. *Polymer* **2011**, *52*, 4528.
(9) Aspbury, P; Wake, W. *Brit. Polym. J.* **1979**, *11*, 17.
(10) Errath, E; Spurr, R. *J. Polym. Sci.* **1959**, *35*, 391.
(11) Gupta, V; Drzal, L; Adams, W; Omlor, R. *J. Mater. Sci.* **1985**, *20*, 3439.
(12) Takahama, T; Geil, P. *Makromol. Chem. Rap. Comm.* **1982**, *3*, 389.
(13) Racich, J; Koutsky, J. *J. Appl. Polym. Sci.* **1976**, *20*, 2111.
(14) Bogdanova, L; Belgovskii, I; Irzhak, V; Rosenberg, B. *Polym. Bull.* **1981**, *4*, 119.
(15) Kreibich, U; Schmid, R. *J. Polym. Sci.* **1975**, *53*, 177.
(16) Matyi, R; Uhlmann, D. J. *Polym. Sci., Polym. Phys. Ed.* **1980**, *18*, 1053.
(17) Duchet, J; Pascault, P. *J. Polym. Sci., Part B: Polym. Phys.* **2003**, *41*, 2422.
(18) Dusek, K; Plestil, J; Lednicky, F; Lunak, S. *Polymer* **1978**, *19*, 393.
(19) Gu, X; Nguyen, T; Ho, D; Oudina, M; Martin, D; Kidah, B; Jasmin, J; Rezig, A; Sung, L; Byrd, E; Jean, Y; Martin, J. *J. Coat. Technol. Res.* **2005**, *2*, 547.
(20) Gu, X; Sung, D; VanLandingham, M; Nguyen, T. *Mater. Res. Soc. Symp. Proc.* **2002**.
(21) Kishi, H; Naitou, T; Matsuda, S; Murakami, A; Muraji, Y; Nakagawa, Y. *J. Polym. Sci., Part B: Polym. Phys.* **2007**, *45*, 1425.
(22) Wu, W; Hunston, D; Yang, H; Sten, R. *Macromolecules* **1988**, *21*, 756.
(23) Mijovic, J; Koutsky, J. *Polymer* **1979**, *20*, 1095.
(24) Morgan, R; O'Neal, J. *J. Mater. Sci.* **1977**, *12*, 1966.
(25) Labana, S; Newman, S; Chompff, A. In *Polymer Networks: Structural and Mechanical Properties*; Chompff, A; Newman, S., Eds.; Plenum: New York, 1971.
(26) Sahagun, C; Morgan, S. *SAMPE 41st ISTC*; Witchita, KS ; SAMPE: Covina, CA, 2009
(27) Sahagun, C; Knauer, K; Morgan, S. *J. Appl. Polym. Sci.* **2012**, in press.
(28) Holm, E. *J. Am. Ceram. Soc.* **1998**, *81*, 455.
(29) Holm, E; Duxbury, P. *Scr. Mater.* **2006**, *54*, 1035.
(30) Holm, E; Meinke, H; McGarrity, E; Duxbury, P. *Mater. Sci. Forum* **2004**, *467–470*, 1039.
(31) Kausch, H. In *Polymer Fracture*: Springer-Verlag: Berlin, 1978.
(32) Friedrich, K. Ph.D. Dissertation Ruhr-Universitat Bochum, Bochum, Germany, 1978.
(33) Franck, A. *APN007*; TA Instruments: New Castle, DE, 2008
(34) Chambon, F; Winter, H. *J. Rheol.* **1987**, *31*, 683.
(35) Winter, H; Chambon, F. *J. Rheol.* **1986**, *30*, 367.
(36) Halley, P; George, G. In *Chemorheology of Polymers*; Cambridge University Press: Cambridge, U.K., 2009.
(37) Menard, K. In *Dynamic Mechanical Analysis*: CRC Press: Boca Raton, FL, 1999.
(38) Pramanik, M; Swanson, J; Scott, J; Mendon, S; Rawlins, J. *SAMPE 41st ISTC*; Witchita, KS ; SAMPE: Covina, CA, 2009.
(39) Min, B; Stachurski, Z; Hodgkin, J; Heath, G. *Polymer* **1993**, *34*, 3620.
(40) Kozielski, K; George, G St.; John, N; Billingham, N. *High Perform. Polym.* **1994**, *6*, 263.
(41) Mijovic, J; Wijaya, J. *Polymer* **1994**, *35*, 2683.
(42) Xu, L; Schlup, J. *J. Appl. Polym. Sci.* **1998**, *67*, 895.
(43) Schechter, J; Wynstra, J; Kurkjy, R. *Ind. Eng. Chem. Res.* **1956**, *48*, 94.
(44) *ASTM D5045: Standard Test Methods for Plane-Strain Fracture Toughness and Strain Energy Release Rate of Plastic Materials* ; ASTM International: West Conshohocken, PA, 1995.
(45) *ASME Standard B46.1–1995: Surface Texture, Surface Roughness Waviness and Lay*; American Society for Mechanical Engineers: New York, 1995.
(46) Ellis, B. In *Chemistry and Technology of Epoxy Resins*: Blackie Academic & Professional: Glasgow, U.K., 1993.
(47) Min, B; Stachurski, Z; Hodgkin, J. *Polymer* **1993**, *34*, 4488.
(48) Riccardi, C; Williams, R. *J. Appl. Polym. Sci.* **1986**, *32*, 3445.
(49) Sahagun, C; Morgan, S. *Polym. Prepr. (Am. Chem. Soc., Div. Polym. Chem.)* **2011**, *52*, 132.